Three-dimensional inversion analysis of an *in situ* stress field based on a two-stage optimization algorithm[*]

She-rong ZHANG[1,2], An-kui HU[1,2], Chao WANG[†‡1,2]

(*1State Key Laboratory of Hydraulic Engineering Simulation and Safety, Tianjin University, Tianjin 300072, China*)

(*2School of Civil Engineering, Tianjin University, Tianjin 300072, China*)

[†]E-mail: wangchaosg@tju.edu.cn

Abstract: Establishing an accurate *in situ* stress field is important for analyzing the rock-mass stability of the underground cavern at the Huangdeng hydropower station in China. Because of the complexity and importance of the *in situ* stress field, existing back analysis methods do not provide the necessary accuracy or sufficiently recognize nonlinear relations between the distribution of the *in situ* stress field and its formative factors. Those factors are related to the geological structures of high compressive tectonic stress regimes, including geological faults and tuff interlayers. The new two-stage optimization algorithm proposed in this paper is a combination of stepwise regression (SR), difference evolution (DE), support vector machine (SVM), and numerical analysis techniques. Stepwise regression is used to find the set of unknown parameters that best match the modeling prediction and determine the range of parameters to be recognized. Difference evolution is used to determine the optimum parameters of the SVM. The SVM is used to create the DE-SVM nonlinear reflection model to obtain the optimal values of the parameters from measured stress data. We compare the new two-stage optimization algorithm to other two popular methods, a multiple linear regression (MLR) analysis method and an artificial neural network (ANN) method, to estimate the *in situ* stress field for the actual underground cavern at the Huangdeng hydropower station. The two-stage optimization algorithm produces a more realistic estimate of the stress distribution within the investigated area. Thus, this technique may have practical applications in realistic scenarios requiring efficient and accurate estimations of the *in situ* stress in a rock-mass.

Key words: *In situ* stress, Stepwise regression (SR), Difference evolution (DE), Support vector machine (SVM), Finite element, Huangdeng underground cavern

http://dx.doi.org/10.1631/jzus.A1600014　　　　　　　　　　　　　　**CLC number:** TU931

1 Introduction

The *in situ* stress field is widely known to be a fundamental factor for not only the analysis, design calculation, and stability assessment of rock engineering projects, but also the study of rock-mass deformation and failure (Guo *et al.*, 1983; Gong *et al.*, 2010). The accuracy of the *in situ* stress field obtained by numerical simulation directly influences the final results, especially for excavations in high level tectonic stress areas (González de Vallejo and Hijazo, 2008). Therefore, it is essential to know the magnitude and direction of *in situ* stress for any underground project before construction, requiring extensive measurements and calculations.

The *in situ* stress field results from a highly complicated process and is affected by many factors, including topography, geological history, the behavioral evolution of rocks, tectonic evolution, the geothermal field, and groundwater. *In situ* measurement is the most direct approach for determining the

geo-stress field (Liu *et al.*, 2014). However, such field tests are often costly and time-consuming. Furthermore, due to the complexity brought by the formation of *in situ* stress and the excessive working impact, the measured results are only a reflection of the local stress field. Thus, based on the measurement results and geological structure conditions, it is crucial to derive a reasonable stress field with wide applicability using a convenient and efficient back analysis approach coupled with an advanced numerical simulation method (Mckinnon, 2001; Saati and Mortazavi, 2011).

In numerical simulations, the *in situ* stress fields are generally acquired by a number of methods using limited measurement and topography data used for design and construction at various engineering sites (Zhang *et al.*, 2006; Guo *et al.*, 2008; Qin *et al.*, 2008). These methods include multiple linear regression (MLR) analysis, artificial neural network (ANN) methods (Kartam *et al.*, 1997; Xu, 2000; Li *et al.*, 2012; Samui *et al.*, 2015), and genetic algorithm optimization approaches, which have been adopted extensively within stress boundary conditions and displacement boundary conditions in particular. However, these methods have unique limitations, specifically in terms of shortcomings in the speed and accuracy of the inverse analysis of the *in situ* stress field.

Under uniform lithology and relatively simple geological conditions, the MLR analysis method for *in situ* stress estimation has been applied in many construction sites to assess the regional *in situ* stress because of its speed and convenience. However, the interaction of the main factors affecting the *in situ* stress field is ignored by the substantial assumptions about linearity and continuity. Moreover, the relationship between the *in situ* stress field and the main factors is too complicated to express by a sub-harmonic multivariate function. Therefore, the MLR analysis method usually lacks conformity with the practical situation and eventually leads to significant inaccuracy. As a typical surrogate direct inversion, the ANN approach attempts to use machine learning to map the nonlinear inverse relationship between the stress measurements and the boundary conditions (Grossberg, 1988; Kartam *et al.*, 1997) but often has difficulty traversing the typically non-convex optimization search space because of its inherent limitations, including non-uniqueness, non-existence, and

instability. Moreover, it relies mostly on a specifically designed algorithm and a high-accuracy digital computer to ensure satisfactory results, often at the expense of convergence speed. Alternatively, the genetic algorithm is a well-known optimization-based approach used to solve the inverse problem to determine the distribution of the *in situ* stress field. However, this method is prone to problems of premature convergence. In other words, it easily converges to a local optimal solution and requires a large number of forward analyses to estimate a solution. This means that it is typically computationally expensive with unnecessary time costs. Moreover, its solution accuracy depends strongly on the selection of the initial population. Given the limitations of these methods, one logical approach is to combine stepwise regression (SR), difference evolution (DE), support vector machine (SVM), and numerical analysis techniques to solve the inverse problem and estimate a stress field that more effectively addresses the need for both accuracy and computational efficiency (Grossberg, 1988; Kartam *et al.*, 1997).

This paper presents the details of a particularly promising approach incorporating linear regression, SVM, and DE, and applies this approach to the problem of inversely obtaining the *in situ* stress field in underground projects. In the following section, considering the effect of the unloading of land surface denudation, we determine a series of parameters to be estimated related to the formation of the rock-mass *in situ* stress field. First, we provide an outline and the technological process of a two-stage optimization algorithm and its incorporation into an inverse solution method, namely the SR-DE-SVM algorithm, for estimating the *in situ* stress in a rock-mass. Then, we use this method to estimate a set of unknown parameters at the underground caverns at the Huangdeng hydropower station, using a numerical analysis to assess the efficacy of the SR-DE-SVM approach. Finally, we present validation tests.

2 Land surface denudation theory for the magnitude of *in situ* stress

2.1 Denudation effect of unloading

In the long term, the geological history and behavioral evolution of rocks may significantly

influence the state of *in situ* stress fields. Some research has shown that the distribution of the rockmass in an *in situ* stress field is strongly influenced by the land surface denudation effects of unloading resulting from an intense geological process when the geological environment is complicated (Hijazo and González de Vallejo, 2012). Consequently, the unloading geological behaviors stemming from land surface denudation must be considered to obtain a reasonable assessment of the *in situ* stress. The *in situ* stress field in high-mountain gorge areas is the inevitable result of various unloading geological behaviors, including land surface erosion and valley denudation, which disequilibrate the state of rockmass stress before the formation of a valley, leading to a new balanced state through the simultaneous adjustment of its stress and strain.

To express the effect of land surface denudation, several reasonable and necessary assumptions should be made, namely, that the land was sufficiently even in ancient times and, based on geological mechanics analysis, that the *in situ* stress comes mainly from gravity and the geological tectonic stress field (Guo, *et al.*, 2008) applied in ancient times. The formation of a rock-mass *in situ* stress field involves many related factors, such as topography, lithology, geological and structural anisotropies, sedimentary loads, tectonic evolution, thermal conditions, and groundwater. However, the thermal stress is equal to only $1/9$ of the gravity stress. Thus, the thermal stress effect on the rock-mass *in situ* stress field is negligible for common underground projects. Conversely, groundwater has an intricate mechanism of influence on the *in situ* stress. Specifically, an increase in pore pressure can reduce the shear strength of the rock in the potential structural plane. Moreover, seepage pressures usually change the *in situ* stress field in underground projects. The thermal conditions and groundwater are usually ignored in analyses because of their comparatively small influence and difficult quantification. The last assumption is that the estimated *in situ* stress field is created by land denudation and erosion in the context of an ancient *in situ* stress field.

2.2 Land surface denudation simulation

Six types of displacement boundary conditions were considered in the simulation analysis to represent the different effects of land surface denudation and river erosion (Fig. 1) (Jiang *et al.*, 2008), reflecting the distribution of the *in situ* stress field under different effects of unloading in underground projects.

3 Two-stage optimization algorithm for estimating inverse *in situ* stress

The two-stage optimization algorithm is a nonlinear global optimization method that combines SR and SVM with DE. It has been shown to be capable of effectively solving global optimization problems with relatively low use of computational resources (Jiang *et al.*, 2013). SR can ascertain the set of unknown parameters that best matches the modeling prediction and determine the range of parameters to be recognized. DE is applied to determine the optimum parameters of the SVM. The SVM is used to create the DE-SVM nonlinear reflection model that maintains the global search capabilities over the whole search space to efficiently determine an optimal solution interval.

3.1 Methodology of the stepwise regression

As a prominent multivariate function, the SR method uses its specific and available efficiency to determine the importance of numerous influencing parameters to obtain the best combination of variables to establish functional relations, especially in a complex system. The selection of the initial parameters strongly influences the evolution velocity of the SVM. Improper parameter selection may lead to generation stagnancy or premature phenomena, failing to satisfy the analysis request. The proposed method introduces SR into the *in situ* stress field inversion analysis to define the causes of the formation of the *in situ* stress more clearly and to provide an important basis for underground cavern design and stability analysis.

Simulation of a tectonic stress field is usually conducted by applying normal or tangential displacement or stress boundary conditions, whose consistency relative to each other is ignored. However, the entry of one factor will lead to degradation of the others. Thus, after calculation and comparison, SR is used to exclude those factors that do not play a
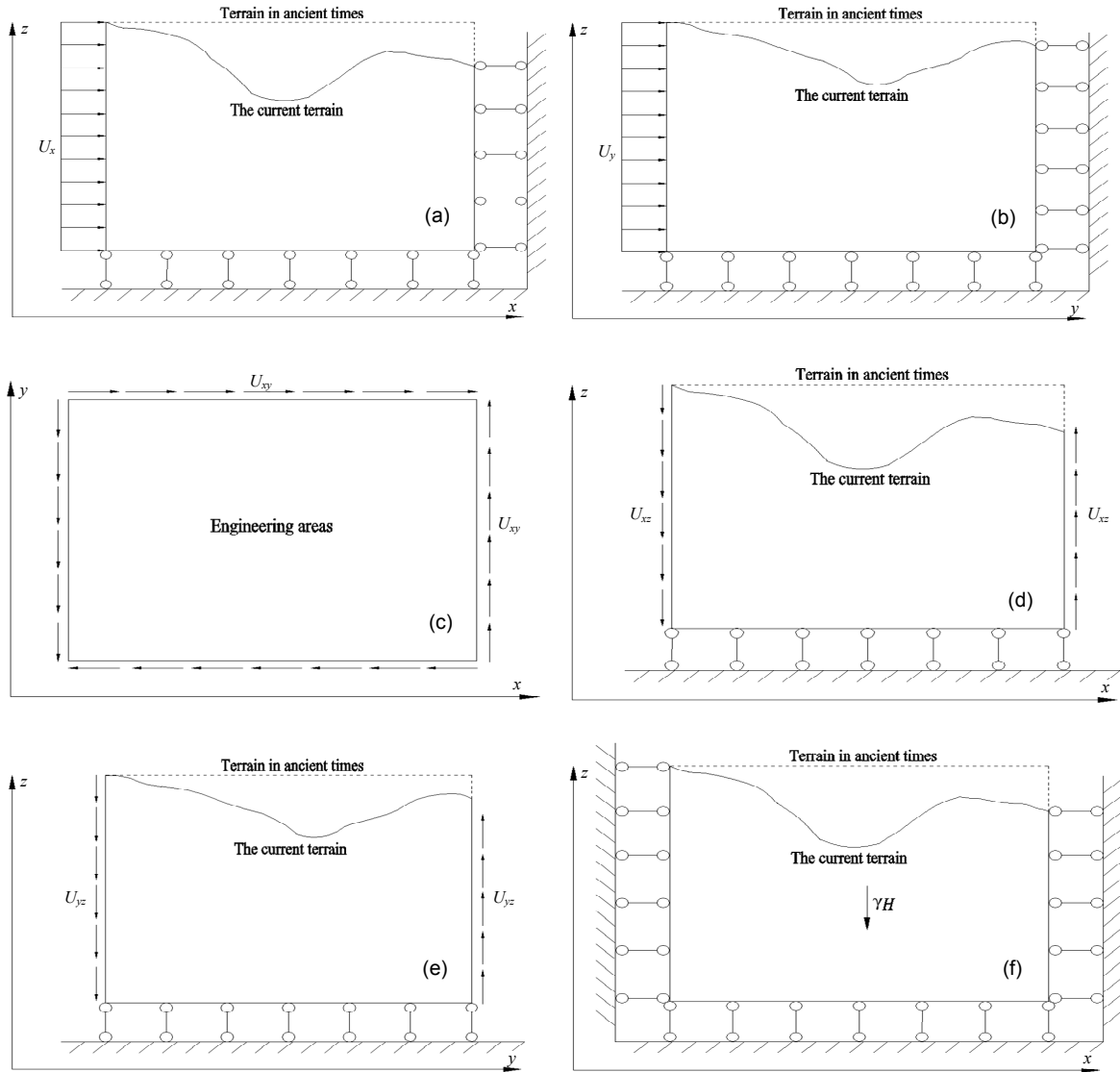
Fig. 1 Schematic diagram of the displacement boundary conditions

(a) Tectonic movement boundary in the x direction, U_x; (b) Tectonic movement boundary in the y direction, U_y; (c) Shear tectonic movement boundary in the xy plane, U_{xy}; (d) Shear tectonic movement boundary in the xz plane, U_{xz}; (e) Shear tectonic movement boundary in the yz plane, U_{yz}; (f) Boundary condition under a gravity function. γ is the unit weight of the rock mass; H is the depth of its location

dominant role in the region of interest. The SR filters and inspects each tectonic stress factor that may be influential and that is consistent with the existing structural features to obtain an optimized solution matching the engineering geological investigation data.

The *in situ* stress value can be represented by the following equation:

$$\sigma_{jk}^0 = C_0 + \sum_{i=1}^{n} C_i \sigma_{jk}^i + \varepsilon, \qquad (1)$$

where σ_{jk}^0 is the calculated initial geo-stress value of stress component j on point k, C_0 is a constant coefficient, C_i represents a stress component caused by each movement pattern, including gravity movement and sub-tectonic movement patterns, σ_{jk}^i is the calculated geo-stress value of stress component j under gravity and sub-tectonic movement on point k, and ε is the model error.

First, we assume that H_0: $C_0 = C_1 = C_2 = \ldots = C_{n-1} = C_n = 0$ and check H_0 using test data as a statistical sample. If H_0 is rejected, the linear regression is

significant, which indicates that a linear relationship exists between the independent and dependent variables. If not, the regression is not significant, which indicates that the regression model does not work.

The core concept of SR is to introduce impact factors one by one under the condition that the factor has an obvious sum of squares of partial regression. The previous factors are then inspected individually after adding new factors to exclude those without obvious relationships, ensuring that the optimal subset of variables can be obtained in several steps. The method is simple and fast because there is no need to determine the partial correlation coefficients.

The least square SR method is adopted to conduct a statistical analysis of the effect of different parameters to be estimated on target parameters. The F-test is applied to check whether the regression is significant, where the statistical magnitude of F has the computational formula shown in Eq. (2). Furthermore, the ratio of the regression sum of squares and the residual sum of squares obeys the distribution F, whose degree of freedom is m and $n-m-1$:

$$F = \frac{U/m}{Q/(n-m-1)} \sim F(m, n-m-1), \qquad (2)$$

where $U = \sum_{k=1}^{n} (\hat{y}_k - \bar{y})^2$ is the regression sum of squares, which is the sum of squares of the difference between the regression value $\hat{y}_k$ and the average value $\bar{y}$, m is the number of variables, n is the sample number, and $Q = \sum_{k=1}^{n} (y_k - \hat{y}_k)^2$ is the residual sum of squares, namely, the sum of squares of the difference between the measured value y_k and the regression value $\hat{y}_k$.

The F statistic can be used to quantify the overall effect of the regression; the larger the F value is, the better the regression equation is. For the given confidence level λ ($\lambda=95\%$ is commonly adopted), the F statistic should satisfy

$$P(F \le F_\lambda(m, n-m-1)) \le 1-\lambda. \qquad (3)$$

If Eq. (3) does not hold, the assumption fails.

The procedure for SR is as follows:

1. Independent variables are adopted to conduct the linear regression statistics for dependent variables and to check the F value.

2. The effect on the dependent variables of the independent variables that are sequentially added to the regression equation is observed. The effect can be determined by both the coefficient of partial correlation between the two variables and the F value regressed by them.

3. If the independent variables introduced earlier become less significant due to the introduction of latter variables, the earlier variables are eliminated.

4. Steps 2 and 3 are repeated until no additional insignificant variables are present in the equation and no additional significant variables are added into the equation. Each time that steps 2 and 3 are repeated, the F value is checked to confirm the significance of the effect of the independent variables on the dependent variables.

3.2 Nonlinear model based on DE-SVM

The SVM is a preeminent machine learning tool that minimizes an upper bound on its expected error. It attempts to convert low-dimensional nonlinear problems into high-dimensional linear problems and then replace inner product computation with a kernel function. More specifically, given data points x_1, x_2, ..., x_n and class labels y_1, y_2, ..., y_n, the SVM has the form:

$$y_i = f(x) = (\boldsymbol{w} \cdot \boldsymbol{x}) + b^* = \sum_{i=1}^{n} (\alpha_i^* - \alpha_i)(x_i \cdot x) + b^*. \qquad (4)$$

Let $\boldsymbol{w}$ be the weighted vector and $x_i \in \mathbb{R}^d$, $y_i \in \mathbb{R}$. Furthermore, let α_i and α_i^* be the support vectors, on which all of the classifications performed by the SVM solely depend. Finally, b^* represents the classification threshold. Thus, an identical SVM would result from a training set that omits all of the remaining examples. The data representation in this feature space need not be explicitly calculated if there is an appropriate Mercer kernel operator for which

$$k(x, x_i) = \exp\left(-\frac{|x - x_i|^2}{2\sigma^2}\right). \qquad (5)$$

A radial basis function is adopted as the typical Mercer kernel operator due to its excellent performance, meaning that the data that are not linearly

separable in the original space may become separable in this feature space. For data sets that are non-separable, slack variables ξ_i and ξ_i^* are introduced to relax the constraint as

$$\min\left[\frac{1}{2}\|\boldsymbol{w}\|^2 + c\sum_{i=1}^{n}(\xi_i + \xi_i^*)\right], \qquad (6)$$

subject to $\xi_i \geq 0$, $\xi_i^* \geq 0$, and $c \geq 0$, representing a constant called the penalty parameter. An optimal model can usually be achieved by seeking the best values of c and k, which play an important role in its prediction accuracy. However, the SVM never provides systematic theoretical approaches for the two parameters.

A DE algorithm is designed to fulfill user requirements, as its control variables are robust and easy to select and it has good convergence to the global minimum in consecutive independent trials (Xing *et al.*, 2015). In this study, we used the advantages of the DE algorithm to explore the best parameters of c and k in SVM modeling due to its simple but efficient global optimization performance (Cheng *et al.*, 2013). The improved DE-SVM algorithm includes the following steps:

1. Initializing of the DE-SVM parameters, which entails randomly generating N_p bivectors about c and k in SVM modeling that should be satisfied to restrain the upper and lower bound independent variables. Because the DE algorithm is designed to be a stochastic real parameter optimization algorithm, its formula is as follows:

$$\boldsymbol{x}_{ij} = \boldsymbol{x}_{ij}^{\mathrm{L}} + \mathrm{rand}(\boldsymbol{x}_{ij}^{\mathrm{U}} - \boldsymbol{x}_{ij}^{\mathrm{L}}), \qquad (7)$$

subject to $i=1, 2, \ldots, N_p$, where N_p represents the population size, $j=1, 2$ is the dimension of the vectors, $\boldsymbol{x}_{ij}^{\mathrm{U}}$ and $\boldsymbol{x}_{ij}^{\mathrm{L}}$ are the upper and lower bound independent variables, respectively, and the function rand is random and rand$\in[0, 1]$.

2. In mutation, the difference between two independent vectors is minimized and then merged with a third independent vector in its population, forming a new variation vector. For the target vector $\boldsymbol{x}_{ij}$, the mutant vector is obtained according to

$$\boldsymbol{v}_{ij}(G+1) = \boldsymbol{x}_{r_1 j}(G) + F(\boldsymbol{x}_{r_2 j}(G) - \boldsymbol{x}_{r_3 j}(G)), \qquad (8)$$

where $r_1, r_2, r_3 \in [1, n]$, which are random indexes. r_1, r_2, and r_3 are chosen to be different from the running index i; thus, $n \geq 4$ to allow for this condition. $F \in [0, 2]$, where F determines the amplification of the differential variation $\boldsymbol{x}_{r_2 j}(G) - \boldsymbol{x}_{r_3 j}(G)$, and G stands for generation.

3. Crossover increases the diversity of the perturbed parameter vectors. Each vector in the current population is combined with a mutant to produce a trial population in this step (Jiang *et al.*, 2013). The trial vectors are expressed as

$$\boldsymbol{u}_{ji,G+1} = \begin{cases} \boldsymbol{v}_{ji,G+1}, & r_j \leq \mathrm{CR} \text{ or } j = rn_i, \\ \boldsymbol{x}_{ji,G}, & r_j > \mathrm{CR} \text{ and } j \neq rn_i, \end{cases} \qquad (9)$$

where $j=1, 2, \ldots, n$; r_j is a random number between 0 and 1; $\mathrm{CR} \in [0, 1]$, called a crossover constant, is determined by the user, and $rn_i \in [1, n]$, which ensures that $\boldsymbol{u}_{ji,G+1}$ obtains at least one vector parameter from $\boldsymbol{v}_{ji,G+1}$.

4. Selection is then performed to determine whether the target or trial vector survives to become a member of the next generation. If the trial vector $\boldsymbol{u}_{ji,G+1}$ yields a smaller cost function value than the target vector $\boldsymbol{x}_{ji,G}$, then the target vector $\boldsymbol{x}_{ji,G}$ can replace the trial vector $\boldsymbol{u}_{ji,G+1}$. That is, the target vector $\boldsymbol{x}_{ji,G}$ is not itself replaced.

5. Loop iteration is conducted, repeating steps 2 to 4, until the end condition for the optimization process is reached. This end condition is set as a maximum generation G_{max} or maximum number of function evaluations, which can be specified by the user to avoid over-fitting. Therefore, the optimal parameters will be obtained when the process reaches the convergence stage, indicating that the optimum parameters are provided for the SVM, allowing it to create an excellent model.

3.3 SR-DE-SVM algorithm

To describe the SR-DE-SVM algorithm as specifically implemented here for the *in situ* stress inverse problem, in which the boundary conditions are set to be unknown parameters and the objective function minimizes the error between the measured stress and the calculated stress at several measurement points, a nonlinear model based on the SVM is

defined as follows:

$$Y = \mathrm{SVM}(X),$$

$$X = (x_1, x_2, \cdots, x_n), \qquad (10)$$

$$Y = (y_1, y_2, \cdots, y_m),$$

where Y is the measured stress of the engineering site, X is the estimated boundary condition, and m and n are the numbers of input variables and output variables, respectively.

Thus, this constrained optimization problem can be expressed as

$$\min E(x_1, x_2, \cdots, x_n) = \frac{1}{m} \sum_{i=1}^{m} (y_i - \mathrm{SVM}_i)^2,$$

$$x_i^{\mathrm{a}} \le x_i \le x_i^{\mathrm{b}}, \quad i = 1, 2, \cdots, n, \qquad (11)$$

where SVM_i represents the stress predicted by the SVM algorithm, and x_i^{a} and x_i^{b} are the upper and lower bounds of x_i, respectively.

Therefore, the objective of the algorithm is to minimize the function min $E(X)$. Fig. 2 shows an overview of the SR-DE-SVM algorithm. The recognition process of the boundary conditions is summarized briefly in the following steps:
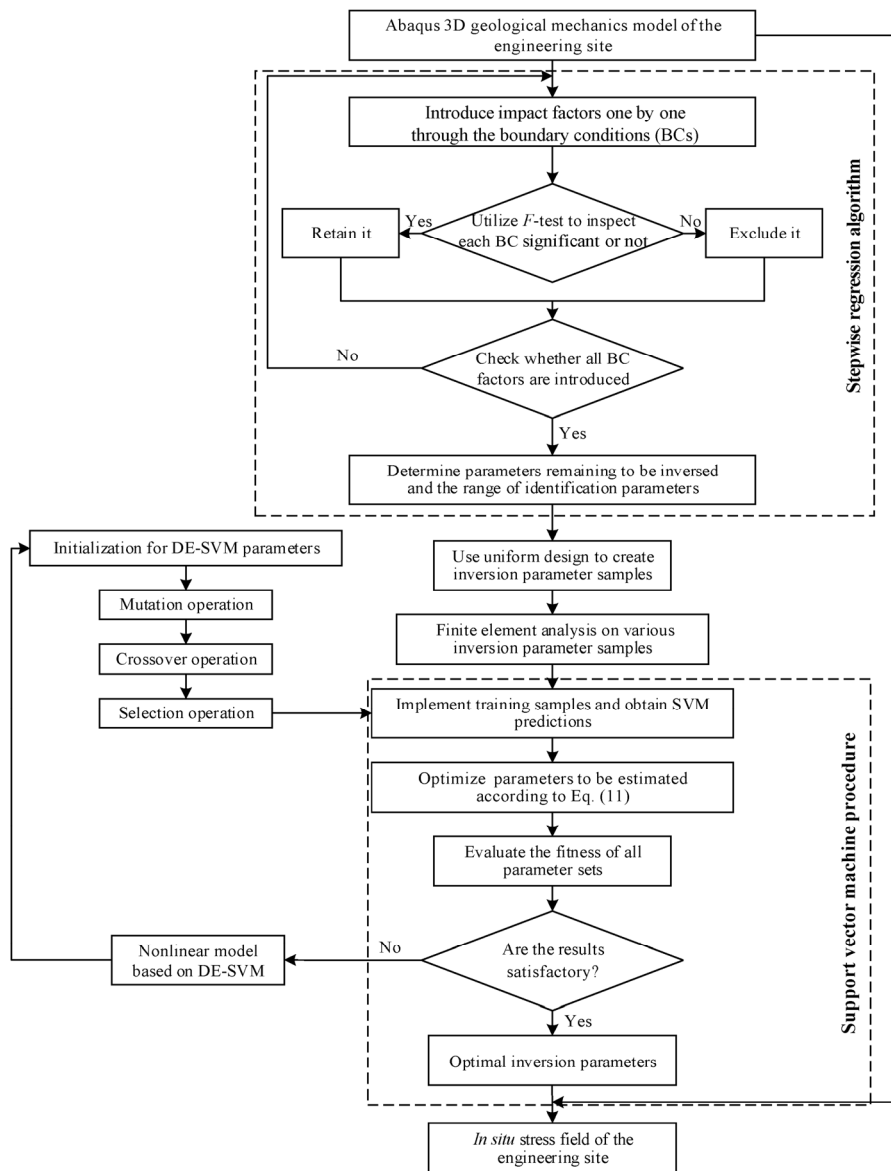

Fig. 2 Flow chart of the SR-DE-SVM algorithm

Step 1: The stepwise regression algorithm attempts to determine the range of parameters to be recognized and the genetic parameters (Feng *et al.*, 2000). This avoids the blindness of the sample generation based on Eq. (1).

Step 2: Inversion parameter samples are created based on uniform design.

Step 3: The 3D geological mechanics model of the engineering site is established completely. After the numerical calculation of each combination of boundary conditions, the corresponding calculated stress is obtained at several measurement points. Each combination of boundary conditions with its corresponding calculated stress comprises a so-called learning sample.

Step 4: Based on the object function, Eqs. (5) and (6), the DE approach is typically used to discover optimal parameters for SVM modeling.

Step 5: A nonlinear model based on DE-SVM is created to describe the relationship between the boundary conditions to be estimated and the actual measured stress.

Step 6: Based on the object function, Eq. (11), the SR-DE-SVM algorithm is used to refine the search using the input-output information generated by the random search. Using the optimal inversion parameters, the distribution of the *in situ* stress field can then be obtained for the engineering site by computerized simulation.

4 Application to the Huangdeng hydropower station

4.1 On-site *in situ* stress measurement in underground cavern zones

4.1.1 Brief description of geological features

The Huangdeng hydropower station is located in Lanping County, Nujiang, Yunnan Province, China. It is part of the fifth stage of a reservoir with seven stations planned along the Lantsang River, and connects the Toba hydropower station upstream to the Dahuaqiao station downstream. Its power generation system is located on the left bank of the station hydropower complex, consisting of the power house, auxiliary plant, transformer chamber, tailrace surge chamber, overhaul gate chamber, pressure tunnels, tailrace branch tunnels, and tailrace tunnels,

with large-scale caverns arranged in a crisscross pattern.

Tectonically, the Huangdeng hydropower station is situated on the east side of overturned synclines and on the west side of overturned anticlines in Kedengjian. The rock stratum runs perpendicular to the river at attitudes of N10°-20°E, NW∠75°-90°. Generally, the rock stratum in the power house, auxiliary plant room, transformer chamber, maintenance chamber of the unit tail water, and the surge tank is composed of metamorphic volcanic breccias, a metamorphic volcanic granule conglomerate mixed with metamorphic tuff, whose rock quality designations (RQDs) are 75%–90% and 60%–75%, respectively, and in the corresponding Q-system for rock mass classification $Q=10–40$ and $Q=1–10$, respectively, in moderately weathered, slightly weathered, and fresh states. Fig. 3 shows the main faults crossed over by the Huangdeng underground cavern group at an elevation of 1480 m, in which five main geological faults, F_9, F_{230-1}, F_{14}, f_{20}, and f_{230-1}, and tuff interlayers t_{p230-1} are a key focus of attention. The rock is relatively intact and slightly permeable, meaning that although the geological conditions are relatively complex in this region, the lithology is rather uniform.
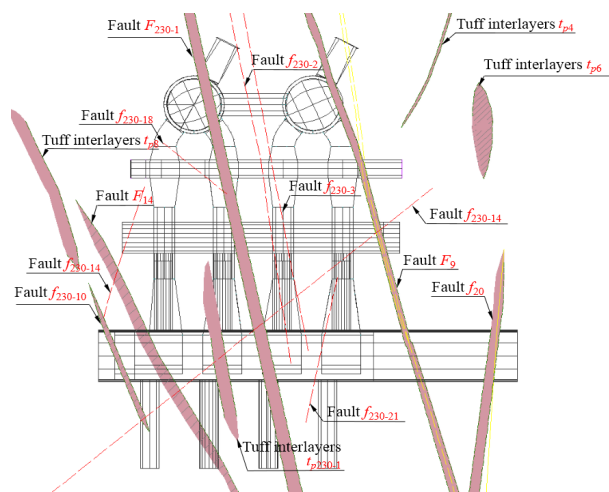

Fig. 3 Main faults crossed over by the Huangdeng underground cavern group at an elevation of 1480 m

Furthermore, the Huangdeng engineering area lies in the secondary tectonic units from the central part of the geosynclinal fold system in Tanggula,

Lanping, and Simao, which is located in the south-western part of the Sichuan-Yunnan rhombic block, and the northern parts of the Indochina and Yunnan-Bruma blocks. The crustal blocks show the characteristics of heterogeneous and asymmetrical uplifting in the whole engineering area. This means that, in general, the terrain is higher in the north and lower in the south. Note that it is part of active structure zones. The direction of fault structures is NNW or trending towards a NS direction, and the faults can be divided into two major types, the Early and Middle Pleistocene and the Quaternary faults. However, no Late Pleistocene faults are found in the underground cavern group zone, and there are no fault structures in the region that might induce a strong destructive earthquake. Moreover, the Huangdeng project is located in the interior of active blocks, and no large or deep active faults cross over the region. Furthermore, it does not lie at the boundary of geotectonic and neo-tectonic areas, and no moderate or intense earthquakes have been recorded. Therefore, on the whole, the Huangdeng engineering region belongs to an area with good structural stability.

4.1.2 Test results and discussion

To study the *in situ* stress distribution of the engineering area, *in situ* stress measurements were made in the underground power house with high-pressure branch pipes using the aperture deforming method with three boreholes. This approach can provide information for the design of the arrangement of the engineering structures, the selection of the excavation methods, and the stability analysis and supporting design of every building. For the disposed *in situ* stress, the aperture distortion needs to be measured, and the 3D *in situ* stress state of the measuring points is obtained according to the relationship between the pitch deformation and the intrinsic *in situ* stress. In the feasibility phase, this project sets four groups of testing points on the left bank of the PD230 exploration audit of the power house and its inferior branch, which are all located at an elevation of 1527.3 m. A sketch map of the *in situ* stress measuring points is shown in Fig. 4. Using the method of aperture deformation with three boreholes, four measured stresses could be obtained: $\sigma_{230\text{-}1}$, $\sigma_{230\text{-}2}$, $\sigma_{230\text{-}3}$, and $\sigma_{230\text{-}4}$. The results are shown in Table 1.
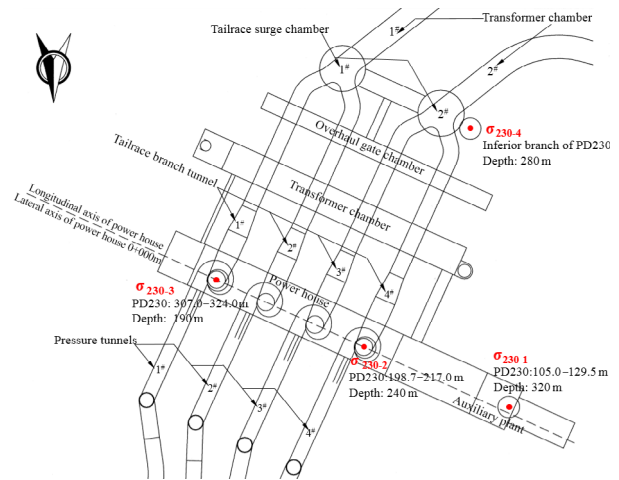
Fig. 4 Layout of the *in situ* stress measuring points in the underground cavern zones

Both Fig. 4 and Table 1 show that, although the maximum, middle, and minimum principal stresses present significantly dispersed features, they still show a certain regularity. As observed from the maximum measured *in situ* stress, the σ_1 values for all measured locations are actually in the pressure stress state, with magnitudes between 7.0 MPa and 15.0 MPa. Furthermore, σ_1 increases as the measuring point depth increases. The values of σ_2 for all measured locations ranged from 2.5 MPa to 7.5 MPa, and those of σ_3 ranged from 1.5 MPa to 5.0 MPa. Moreover, the measured maximum principal stress σ_1 was consistent in its direction, which was south-north or east-west, with a dip angle of S15°-40°E with a positive gradient slope. Its dip angle was slightly smaller than its slope angle, which decreased as the point depth increased.

Generally, the angle ϕ between the direction of the measured maximum principal stress σ_1 and the longitudinal axis of the power house should be kept within 15°–30°, according to statistical data from several in-built underground cavern projects in China (Table 2). As Table 1 shows, the direction of the measured maximum principal stress σ_1 is S39.7°E. Therefore, the direction of the longitudinal axis of the power house is determined as NW294.5°. Considering the influence of the geological conditions of the engineering area and the overall coordination of the project, this means that the angle ϕ is equal to 25.8°. We conclude that the angles between the direction of the measured maximum principal stress σ_1

**Table 1 Principal stress results from *in situ* stress measurements in the underground cavern zones**

Test point	Location	σ_1			σ_2			σ_3		
		Stress (MPa)	Orientation	Dip angle (°)	Stress (MPa)	Orientation	Dip angle (°)	Stress (MPa)	Orientation	Dip angle (°)
$\sigma_{230\text{-}1}$	PD230: 105.0–129.5 m; depth: 320 m	6.97	S36.4°E	39.7	2.49	N35°E	21.0	1.77	S76°E	−42.9
$\sigma_{230\text{-}2}$	PD230: 198.7–217.0 m; depth: 240 m	11.88	S12.6°E	34.3	6.17	N58.2°E	25.7	3.28	S60.2°E	−44.7
$\sigma_{230\text{-}3}$	PD230: 307.0–324.0 m; depth: 190 m	14.63	S39.7°E	18.2	5.02	N86.3°E	−60.7	1.82	N42.6°E	22.1
$\sigma_{230\text{-}4}$	Inferior branch of PD230; depth: 280 m	13.25	S40.5°E	22.7	7.24	S81.5°E	−61.0	4.81	N42.1°E	17.1

Table 2 Statistical data from several in-built underground cavern projects in China

Engineering project	σ_1		Orientation of longitudinal axis of power house	ϕ (°)
	Stress (MPa)	Orientation		
Ertan	64.4	N23°E	N6°W	29
Xiaolangdi	5.0	N20°E	N10°W	30
Lubuge	19.0	N70°W	N45°W	25
Guangzhou Pumped Storage	12.2	Nearly EW	N80°E	Nearly parallel
Xiaowan	23.0	N64°W	S140°E	24
Nuozhadu	8.27	N50.1°-55.8°E	N76°E	20.2–25.9

and the longitudinal axis of the transformer chamber and the tailrace surge chamber are acute angles, which is beneficial to the stability of the whole underground cavern group.

Fig. 5 plots a large dataset of stress magnitudes versus depth based on national data from typical hydropower projects in China, including the Huangdeng hydropower station, and shows the minimum and maximum envelope lines reported by different researchers (Feng *et al.*, 2000; Xue and Chen, 2006; Zhao *et al.*, 2007; Zhang, 2011; Li *et al.*, 2012; Liu *et al.*, 2014). The K values have been calculated as defined by Brown and Hoek (1978), $K=(\sigma_H+\sigma_h)/(2\sigma_V)$, to compare the envelope lines expressed by scatter points in Fig. 5, and σ_H and σ_h represent horizontal stresses in two directions of a particular plane, while σ_V represents the vertical stress. The four solid scatter points represent the actual *in situ* stress measurements of the Huangdeng hydropower station. Table 3 shows the relationship among K_H, K_h, and depth for the other main hydropower projects in China, defining $K_H=\sigma_H/\sigma_V$ and $K_h=\sigma_h/\sigma_V$. The maximum envelope lines are generally similar, with less data scatter for
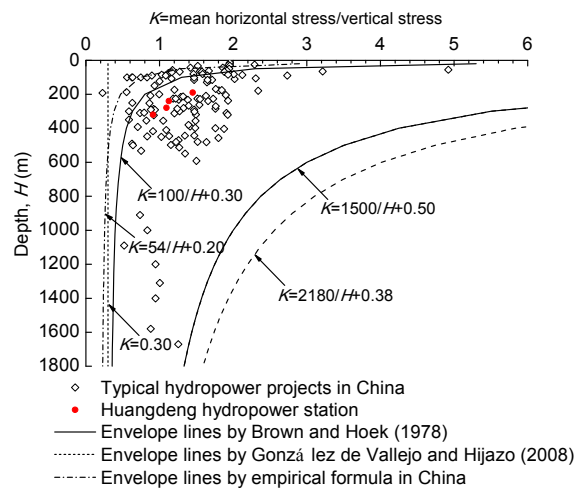
Fig. 5 K-depth relationships based on national data for China

depths greater than 1000 m, with K tending toward 1.0 with depth. The minimum envelope lines show greater discrepancies for depths below 500 m. These results show that at typical depths for most underground excavations, K-depth relationships cannot be used in practice.

**Table 3 *K*-depth relationships for typical hydropower projects in China**

Typical engineering project	K_H	K_h	K	Depth (m)
Three Gorges (Feng *et al.*, 2000)	2.50	2.11	2.31	106.0
	1.42	1.10	1.26	235.0
	0.70	0.55	0.63	490.0
	0.52	0.52	0.52	1090.0
Nuozhadu	0.81	0.30	0.55	187.4
	1.77	1.00	1.39	232.8
Longtan	1.35	1.20	1.28	67.5
	2.88	0.74	1.81	177.0
Xiluodu	2.09	1.17	1.63	210.0
	1.41	0.44	0.92	324.0
	1.57	0.69	1.13	445.0
Jinping I (Gong *et al.*, 2010)	0.84	0.63	0.74	910.0
	1.22	0.79	1.01	1310.0
	1.58	0.93	1.26	1670.0
Xiaolangdi	1.05	1.01	1.03	85.0
	1.07	0.42	0.75	100.0
	1.03	0.83	0.93	149.0
Rasiva	1.48	0.31	0.90	90.0
	2.04	1.39	1.72	115.0
	1.22	0.77	1.00	200.0
	0.89	0.58	0.74	310.0
	1.30	0.88	1.09	410.0
Dagang-shan	1.85	0.98	1.42	390.0
	1.43	0.62	1.03	450.0
	1.06	0.22	0.64	500.0
Baihetan	1.95	0.99	1.47	290.0
	1.57	1.42	1.49	320.0
	1.72	1.22	1.47	442.0
	1.37	1.17	1.27	513.0
	1.76	1.24	1.50	591.5
Pubugou (Xue and Chen, 2006)	1.76	0.83	1.29	215.0
	1.87	0.93	1.40	267.0
	1.36	1.04	1.20	312.0
	1.39	0.97	1.18	57.3
	1.71	1.84	1.78	125.0
	1.72	1.38	1.55	228.0
	1.40	1.15	1.27	300.0

4.2 Numerical calculation model

Having comprehensively considered many factors, such as the characteristics of topography and geomorphology, an elaborate numerical simulation model was built based on the characteristics of the layout and structure of the actual engineering project. Particular attention was paid to the modeling range, affected zones, and boundary constraint conditions of the Huangdeng underground cavern group. The scope of the computational model was 478 m in the *x*-direction, 450 m in the *y*-direction, and 596 m from the isolated rock-mass, to eliminate the effect of artificial boundary errors on the structure of the underground caverns (Fig. 6). There are more than 104 583 nodes and 618 027 quadrilateral elements in this numerical calculation model, including five main geological faults, F_9, F_{230-1}, F_{14}, f_{20}, and f_{230-1}, and tuff interlayers t_{p230-1} located in the underground cavern area.

The Mohr-Coulomb model was adopted in the Abaqus analysis. In the inversion of the *in situ* stress field, the simulation of land surface denudation mainly entails taking the highest point of the calculated region as a baseline, which is necessary to choose an appropriate region. Gravity stress revises the coefficient parameter of the volume-weight to serve as an influence parameter that is expected to be output; tectonic stress is created by applying the displacement boundary in the computing area. A gradual elastoplastic excavation simulation is adopted to record the denudation effect of unloading. Because roller boundary conditions are reasonable for the pre-excavation process of the *in situ* stress field inversion (Zhao *et al.*, 2012), the bottom edge constraint is applied for normal constraints, while the outer boundary of the rock formation is considered to be a free boundary (Zhang and Yin, 2014). The
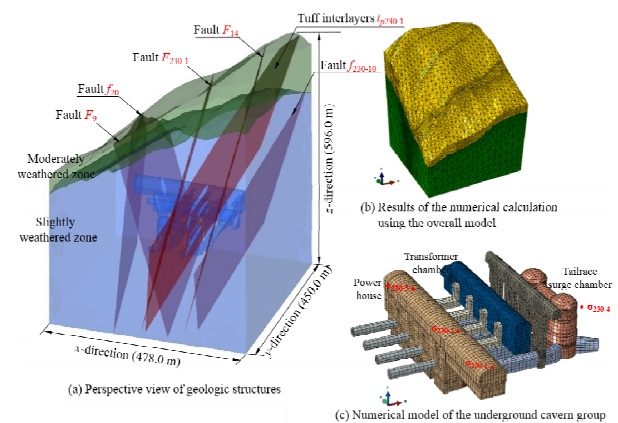
Fig. 6 Numerical simulation model of the Huangdeng underground cavern group

physical and mechanical properties of the rock-mass used in the numerical experiment, which are taken mainly from the results of previous laboratory tests, are given in Table 4. In other words, the whole process of numerical simulation follows the principle of geometry simulation, constitutive simulation, and stress state simulation.

4.3 Recognition of the boundary conditions to be determined

4.3.1 Process of undetermined parameter recognition

Based on the coordinate system of the numerical simulation model, the principal stress results from the *in situ* stress measurements were converted into stress components (Table 5). The SR-DE-SVM method is proposed to obtain optimal values of parameters that best match the modeling prediction with the measured stress data. Specifically, the appropriate boundary conditions for the numerical calculation model, such as the gravity correction coefficient and various tectonic movement patterns, are recognized. SR is used to search for the best parameter system, having a decisive role in the formation process of the *in situ* stress field, which is expressed using the *C#* programing language. Based on the results of SR analysis, the shear structure factors τ_{xy} and τ_{yz} were regarded as unsatisfactory results under

the boundary conditions. In other words, five undetermined parameters were defined in the inversion analysis, including the gravity correction coefficient g^* and other shear structure factors τ_{xx}, τ_{yy}, τ_{yx}, and τ_{xz}. Furthermore, the ranges of identification parameters were determined as follows: $g^* \in [7.85, 17.66]$ m/s^2, $\tau_{xx} \in [0.10, 0.25]$ m, $\tau_{yy} \in [0.00, 0.15]$ m, $\tau_{yx} \in [0.25, 0.45]$ m, and $\tau_{xz} \in [0.10, 0.25]$ m. Finally, 35 training and test samples with the calculated stress components at measured points and undetermined parameters of boundary conditions were created by uniform design $U_{35}(35^3)$.

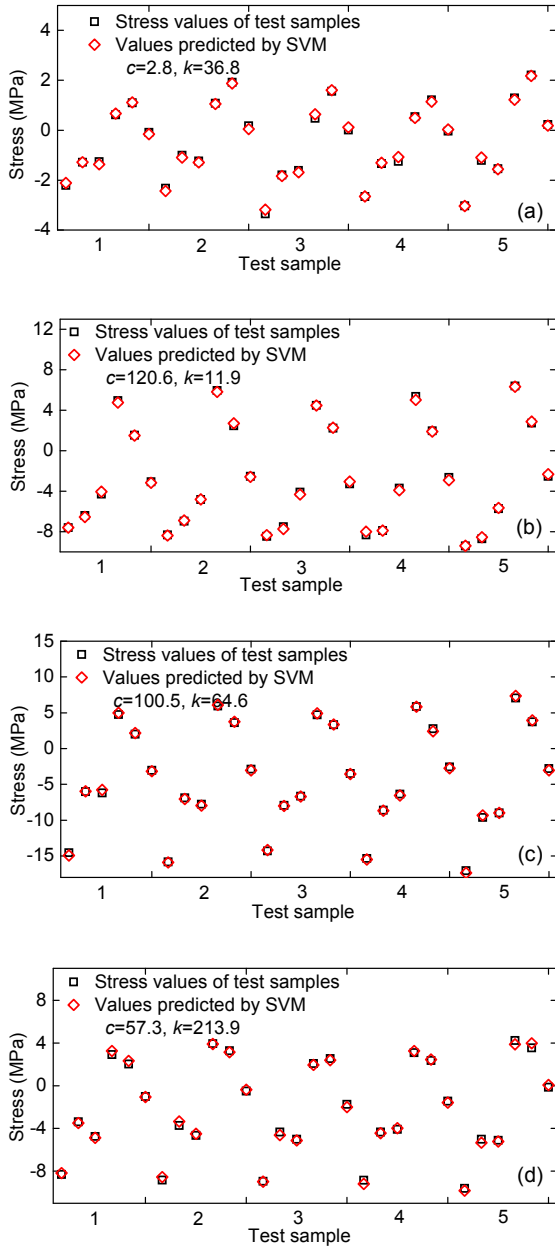4.3.2 Process of undetermined parameter recognition

In this section, the results of the proposed DE-SVM method are verified against the data generated in Section 4.3.1. Taking 30 schemes as training samples and five schemes as test samples, the DE-SVM algorithm can be used to obtain the best parameters of *c* and *k* in SVM modeling. After conducting learning and training using the corresponding parameters input from the training samples, a nonlinear mapping model was established between the measured stress of the engineering site and the boundary conditions to be estimated. Fig. 7 shows the forecast effect tests of SVM for five test samples. The tendency is for the predictions by SVM to be close to the stress values

Table 4 Physical properties of the rock-mass applied in the numerical model

Lithology	Unit weight (kN/m^3)	Elastic modulus (GPa)	Poisson's ratio	Cohesion strength (MPa)	Fiction angle (°)	Dilatancy angle (°)
Moderately weathered zone	26.3	12.0	0.27	1.1	47.8	28.8
Slightly weathered zone	26.5	13.0	0.26	1.2	50.2	33.5
Tuff interlayers t_{p230-1}	25.5	8.0	0.29	0.9	42.0	15.0
Fault F_9	25.0	2.0	0.30	0.2	35.0	8.3
Fault f_{20}	25.5	6.0	0.28	0.3	42.0	10.4
Fault F_{230-1}	25.0	2.0	0.30	0.1	26.6	6.6
Fault F_{14}	25.0	2.0	0.30	0.2	32.0	7.5
Fault f_{230-10}	25.5	6.0	0.28	0.3	38.7	9.7

Table 5 Stress components of *in situ* stress measurement in the underground cavern zone

Test point	Location	Stress component (MPa)					
		σ_x	σ_y	σ_z	τ_{xy}	τ_{xz}	τ_{yz}
σ_{230-1}	PD230: 105.0–129.5 m; depth: 320 m	−4.14	−3.11	−3.98	1.20	2.28	−1.01
σ_{230-2}	PD230: 198.7–217.0 m; depth: 240 m	−6.14	−8.64	−6.56	1.74	3.04	−2.25
σ_{230-3}	PD230: 307.0–324.0 m; depth: 190 m	−11.79	−4.18	−5.50	4.21	2.22	−2.30
σ_{230-4}	Inferior branch of PD230; depth: 280 m	−11.24	−6.14	−7.93	2.60	1.73	−1.55

compared with those obtained by an MLR analysis method and an ANN method to estimate the *in situ* stress field for the actual underground cavern at the Huangdeng hydropower station. Fig. 8 shows the three algorithms used to explore the boundary conditions.

Fig. 8 Various algorithms used for boundary condition exploration

First, a nonlinear model based on DE-SVM was introduced to the objective function, Eq. (12), to explore the best matched values of the boundary conditions. Based on the results of SR, the initial values of five optimization variables were set as follows: $g^* = 11.78$ m/s^2, $\tau_{xx}=0.18$ m, $\tau_{yy}=0.08$ m, $\tau_{yx}=0.35$ m, and $\tau_{xz}=0.15$ m. The population size N_p was 20, and the maximum number of iterations G_{max} was 500. The value of the scaling factor F strongly influences the rate of convergence and the crossover constant CR in the optimized recognition process, both of which are determined by the user. Fortunately, the convergence value tends to be stable, which means that there is almost no difference for different values of F and CR. When the DE curve became astringed, the optimal undetermined parameters were obtained (Table 6). The inversion results of the MLR and ANN methods are also presented for comparison.

Because of the limited number of measuring points, the MLR and ANN methods, which are widely applied, were selected to provide a reasonable comparison with the SR-DE-SVM algorithm. The procedure used in this study showed superior accuracy and efficiency in the inversion analysis of the *in situ* stress field. To verify the rationality of the identification parameters, the obtained boundary conditions of different algorithms were input into a numerical calculation model for elastic-plastic finite element analysis. Tables 7 and 8 show the computational stress components at four monitoring points.

Fig. 7 Forecast effect tests of measured points by SVM
(a) $\sigma_{230\text{-}1}$; (b) $\sigma_{230\text{-}2}$; (c) $\sigma_{230\text{-}3}$; (d) $\sigma_{230\text{-}4}$

of the testing samples, meaning that the nonlinear relationship between the measured stress and unknown boundary conditions can be reflected by a nonlinear model based on DE-SVM.

4.3.3 Definition of boundary conditions

In this section, the optimal values of the parameters from the measured stress data obtained using the SR-DE-SVM nonlinear reflection model are

Table 6 Stress components of the *in situ* stress measurement in the underground cavern zone

Algorithm	Parameter to be recognized						
	τ_{xx} (mm)	τ_{yy} (mm)	τ_{xy} (mm)	τ_{yx} (mm)	τ_{xz} (mm)	τ_{yz} (mm)	g^* (m/s^2)
MLR	23.4	15.0	−9.3	25.6	−15.0	16.8	14.7
ANN	19.2	13.6	−9.8	36.2	−6.0	14.3	13.5
SR-DE-SVM	24.5	12.4		38.2		18.6	15.9

Table 7 Computational stress components at four monitoring points

Test point	Algorithm	Stress component (MPa)					
		σ_x	σ_y	σ_z	τ_{xy}	τ_{xz}	τ_{yz}
σ_{230-1}	Monitored	−4.14	−3.11	−3.98	1.20	2.28	−1.01
	MLR	−6.03	−4.49	−3.67	1.02	1.92	−0.24
	ANN	−4.89	−3.72	−3.87	1.09	1.99	−0.57
	SR-DE-SVM	−4.47	−2.93	−4.08	1.32	1.98	−0.99
σ_{230-2}	Monitored	−6.14	−8.64	−6.56	1.74	3.04	−2.25
	MLR	−9.53	−11.02	−6.30	1.56	2.87	−2.92
	ANN	−8.35	−10.00	−6.48	1.69	3.09	−2.56
	SR-DE-SVM	−6.02	−8.89	−6.21	1.42	3.36	−2.47
σ_{230-3}	Monitored	−11.79	−4.18	−5.50	4.21	2.22	−2.30
	MLR	−13.43	−5.57	−7.98	2.10	2.95	−2.47
	ANN	−12.58	−4.66	−6.65	3.20	2.56	−2.44
	SR-DE-SVM	−12.05	−3.91	−6.00	4.49	2.42	−2.63
σ_{230-4}	Monitored	−11.24	−6.14	−7.93	2.60	1.73	−1.55
	MLR	−10.05	−7.33	−6.65	0.35	2.40	−1.35
	ANN	−10.60	−6.90	−7.45	3.33	1.08	−1.52
	SR-DE-SVM	−11.49	−6.49	−7.96	2.03	1.92	−1.38

Table 8 Computational stress components at selected nodes

No.	Nodes number	Algorithm	Stress component (MPa)					
			σ_x	σ_y	σ_z	τ_{xy}	τ_{xz}	τ_{yz}
A	103 052	MLR	−7.74	−8.48	−4.73	−0.17	3.73	−1.80
		ANN	−8.81	−9.05	−7.00	−0.31	3.58	−2.20
		SR-DE-SVM	−8.10	−8.32	−5.37	−0.25	3.21	−1.93
B	102 432	MLR	−4.62	−6.10	−4.34	1.71	1.61	−0.59
		ANN	−5.45	−7.49	−4.82	1.86	1.69	−0.32
		SR-DE-SVM	−4.82	−7.20	−4.79	1.81	1.65	−0.60
C	25 786	MLR	−14.08	−9.28	−10.47	4.65	2.39	−3.06
		ANN	−14.53	−10.22	−10.47	4.85	2.36	−3.16
		SR-DE-SVM	−14.20	−8.71	−10.44	4.76	2.38	−3.07
D	31 435	MLR	−10.49	−7.88	−8.27	0.46	2.57	−1.66
		ANN	−10.56	−7.94	−8.27	0.44	2.51	−1.66
		SR-DE-SVM	−10.95	−7.83	−8.28	0.49	2.56	−1.74
E	102 811	MLR	−15.07	−10.25	−11.64	8.84	1.82	−3.01
		ANN	−16.88	−10.68	−13.82	8.94	1.57	−5.25
		SR-DE-SVM	−15.58	−10.68	−12.56	8.31	1.82	−4.44
F	102 338	MLR	−10.55	−8.44	−9.51	0.45	−0.45	0.17
		ANN	−12.68	−9.47	−10.75	0.30	−0.42	0.16
		SR-DE-SVM	−11.63	−9.35	−10.3	0.33	−0.37	0.15

Fig. 9 compares the normal stress at each of the four monitoring points with three different results respectively, while Fig. 10 compares the normal stress at each of the six selected nodes A–F, which were chosen on Pile No. K0+070 m cross section in the *x*-direction (Fig. 11).

The results of each algorithm are in good agreement with the monitored *in situ* stresses, especially for the ANN and SR-DE-SVM methods. Furthermore, note that for each of the six selected points, the results of all the algorithms are very consistent. Thus, the efficiency and error comparison of MLR, ANN, and SR-DE-SVM in Table 9 shows that the three methods have a similar time cost for model
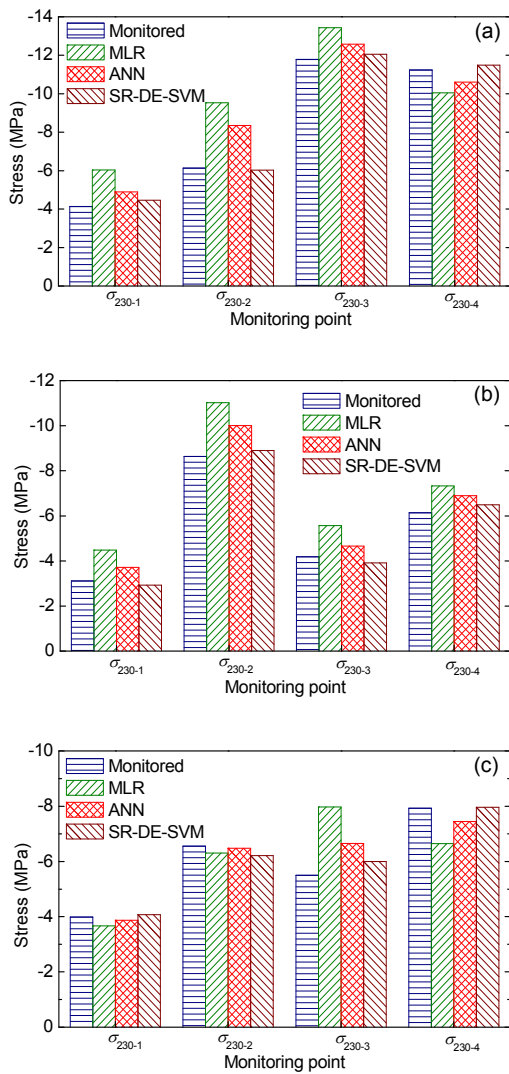
Fig. 9 Comparison of normal stress at each of the four monitoring points: (a) σ_x; (b) σ_y; (c) σ_z
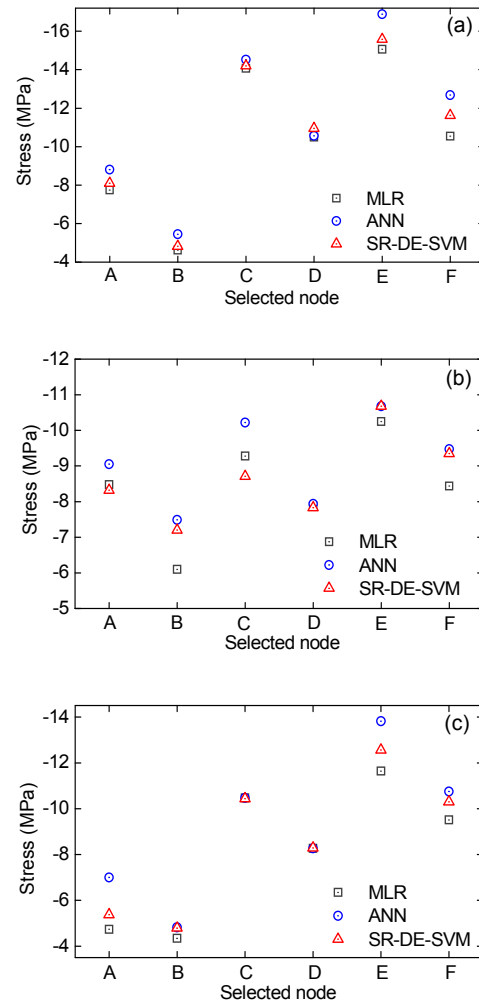

Fig. 10 Comparison of normal stress at each selected node: (a) σ_x; (b) σ_y; (c) σ_z

building. However, the computing analysis time of the SR-DE-SVM algorithm was only 4489 s, compared with 6236 s for MLR and 5816 s for ANN due to the reduction in the parameters of boundary conditions to be applied greatly improving efficiency. More importantly, the model performance of SR-DE-SVM appears to provide the best match, with a maximum absolute error of only 1.50 MPa and a maximum relative error of only 9.09%.

4.4 Distribution analysis of the *in situ* stress field

The distribution of the *in situ* stress field at the Huangdeng engineering site was successfully obtained after optimal boundary conditions from the SR-DE-SVM algorithm were input into a numerical

calculation model for elastic-plastic finite element analysis.

4.4.1 Characteristics of vertical subsidence and horizontal displacement

Based on the power house excavation from step 1 through step 6, the curves of vertical subsidence (Fig. 12) and horizontal displacements (Fig. 13) in different excavation stages are shown to facilitate the comparative study under different stress fields, including an ideal gravity stress field and the estimated and practical *in situ* stress field.

In the ideal gravity stress field, the subsidence curves of the selected analysis baseline in the Huangdeng numerical calculation model are smooth and symmetrical (Fig. 12a). With increasing excavation depth, the subsidence increases markedly, and the maximum subsiding center migrates slowly to the longitudinal axis of the power house.
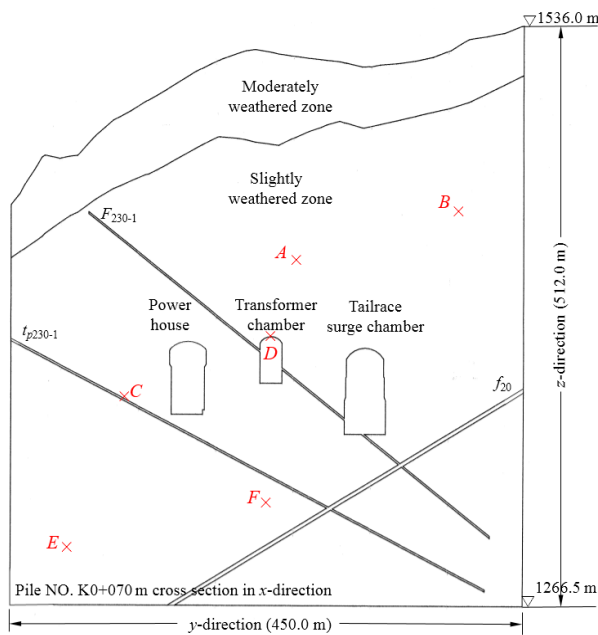
In the estimated and practical *in situ* stress field, the subsidence curves of the selected analysis baseline show different characteristics at different excavation stages (Fig. 12b). In the initial stage of single-level excavation, although the subsidence curves are similar, the maximum subsidence value is only 72.8% of those in the gravity stress field. In the subsequent excavation steps, the maximum subsiding center gradually migrates from the primary longitudinal axis to the upstream side of the power house (the left side of the coordinate) with excavation depth during the excavation process. Moreover, the subsidence values are all larger than those of each excavation step in the ideal gravity stress field. This means that the migration rate is larger in the estimated and practical *in situ* stress field than in the
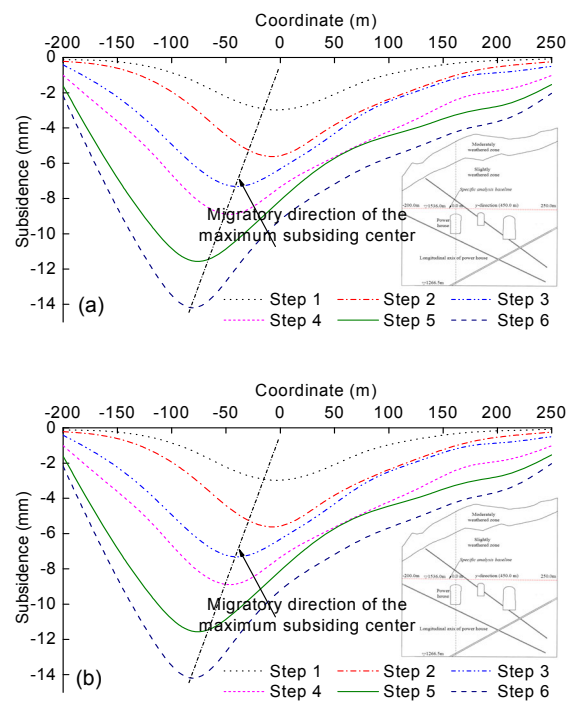

Fig. 11 Selected nodes on Pile No. K0+070 m cross section in the *x*-direction

Fig. 12 Curves of subsidence induced by excavation in an ideal gravity stress field (a) and the estimated and practical *in situ* stress field (b)

Table 9 Model efficiency and error comparison in the recognition of boundary conditions

Algorithm	Efficiency (s)				Error	
	Build	Train	Test	Computing analysis	Max. absolute error (MPa)	Max. relative error (%)
MLR	360	6.62	0.01	6236	3.39	55
ANN	410	0.92	0.02	5816	2.21	36
SR-DE-SVM	384	0.90	0.19	4489	0.50	9.1

gravity stress field, and the maximum subsidence increases 21.7% compared with the latter. Thus, the tectonic stress field is closely linked to the displacement field as well as the stability of the surrounding rock-mass in the engineering site, which appears to be non-negligible.

The horizontal displacements changed at different stages of excavation in different stress fields (Fig. 13). In general, the horizontal displacements of the downstream side of the power house (the right side of the coordinate) were much larger than those of the upstream side in the ideal gravity stress field. Furthermore, the maximum horizontal displacement of the downstream side of the power house was 2.24 times that of the upstream side in the gravity stress field (Fig. 13a). In contrast, the maximum horizontal displacement of the downstream side of the power house was only 1.59 times that of the upstream side in Fig. 13b, but the horizontal displacement and its distribution range expanded prominently because of the occurrence of the practical tectonic stress field.
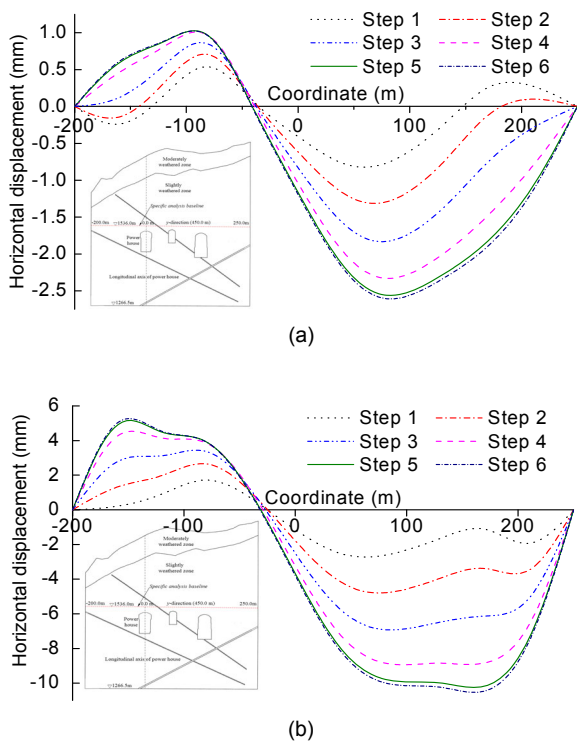
4.4.2 Characteristics of *in situ* stress in the area of the power house along its depth

Taking the power house as an example, Fig. 14 shows the distribution curves of the normal stresses σ_H, σ_h, and σ_V of the selected analysis baseline (the longitudinal axis of the power house) along its depth. With increasing rock-mass depth, the normal stresses σ_H, σ_h, and σ_V increase linearly in the area of the underground rock-mass without geological faults as well as in those with tuff interlayers incised. In detail, σ_H ranges from 10.5 MPa to 15.1 MPa in the buried depth range of the Huangdeng underground cavern group, while σ_h is between 7.45 MPa and 11.3 MPa, and σ_V is between 7.36 MPa and 12.0 MPa. Thus, the change rate of the vertical stress σ_V seems to be more sensitive to the increase in the rock-mass depth. Around the surface area of the rock-mass, the *in situ* stress follows the size relationship of each normal stress $\sigma_V<\sigma_h<\sigma_H$, but when the buried depth exceeds a certain value of 200 m, the relationship changes to $\sigma_h<\sigma_V<\sigma_H$.
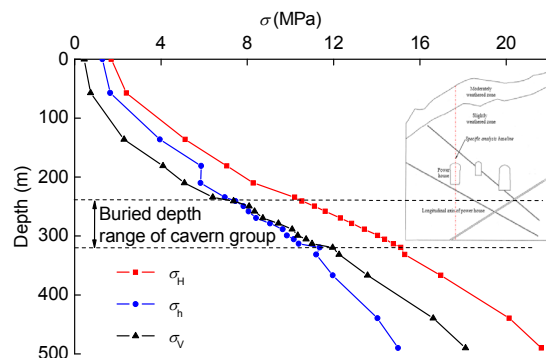
Fig. 14 Distribution of *in situ* stress in the area of the power house along its depth

Furthermore, Fig. 15 shows the distribution curves of K_H and K_h of the selected analysis baseline (the longitudinal axis of the power house) along its depth. K_H and K_h decrease gradually with increasing rock-mass depth, with a particularly sharp decrease near the surface of the rock-mass. The decrease rates of K_H and K_h are relatively stable in the buried depth range of the Huangdeng underground cavern group, with $K_H\in(1.26, 1.43)$, and $K_h\in(0.94, 1.01)$.

σ_H ranges from 10.5 MPa to 15.1 MPa in the buried depth range of the Huangdeng underground

Fig. 13 Curves of the horizontal displacement induced by excavation in an ideal gravity stress field (a) and the estimated and practical *in situ* stress field (b)

cavern group, while σ_h and σ_V are between 7.45 MPa and 11.3 MPa, and between 7.36 MPa and 12.0 MPa, respectively. Thus, the change rate of the vertical stress σ_V seems to be more sensitive to the increase in the rock-mass depth. The influence mechanism of the tectonic movements to the *in situ* stress field is more complicated closer to the surface of the rock-mass, which ultimately results in the instability of K. Therefore, prioritizing K for a rock-mass whose buried depth exceeds 200 m, the function of the optimum regression curve is reasonably expressed by the formula $K=105/H+0.80$, which is highly consistent with the relevant results of Zhao *et al.* (2007).

5 Validation tests: Nuozhadu underground cavern groups

Validation tests were conducted by comparing the results produced by the SR-DE-SVM algorithm and the measured *in situ* stresses in the Nuozhadu underground cavern groups. The *in situ* measurements
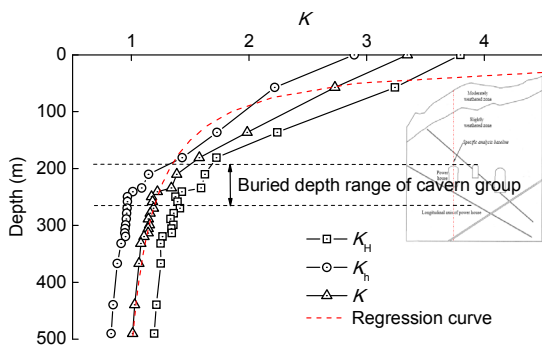
of the Nuozhadu underground cavern groups were made by the Hydro-China Kunming Engineering Corporation. As the measured *in situ* stresses show (Table 10), the stress level is low in general, because the buried depth of the underground cavern is not very deep. The magnitude and direction of *in situ* stress are influenced mainly by the geological structure, topography of the engineering area, and the gravity stress field. The numerical analysis was simulated using the SR-DE-SVM algorithm in the Abaqus codes. Table 10 compares the measured *in situ* stresses with results produced by the SR-DE-SVM algorithm in the Nuozhadu underground cavern group. Fig. 16 compares the normal stress at each of the four monitoring points in the Nuozhadu underground cavern group intuitively. The results demonstrate high precision of the *in situ* stress field in the Nuozhadu underground cavern area, which means that the *in situ* stress distribution within the engineering area can be estimated effectively using the SR-DE-SVM algorithm.

6 Conclusions

Due to the complexity and importance of the *in situ* stress field, it is necessary to learn about the magnitude and direction of an *in situ* stress field for any underground project according to its specific geological conditions. The SR-DE-SVM algorithm, which is a nonlinear global optimization method combining SR, DE, SVM, and numerical analysis techniques, was presented for estimating the *in situ* stress in the rock-mass. Through the example of the Huangdeng hydropower station, the SR-DE-SVM

Fig. 15 Distribution of K in the area of the power house along its depth

Table 10 Comparison between the measured *in situ* stresses and results produced by the SR-DE-SVM algorithm in the Nuozhadu underground cavern group

| Test point	Vertical depth (m)	Algorithm	Stress component (MPa)					
			σ_x	σ_y	σ_z	τ_{xy}	τ_{xz}	τ_{yz}
$\sigma_{204-302}$	232.8	Monitored	−4.34	−7.72	−4.36	−1.61	−2.86	2.46
		SR-DE-SVM	−4.25	−7.86	−4.31	−1.87	−2.53	2.04
$\sigma_{204-502}$	207.3	Monitored	−0.93	−5.98	−3.95	2.35	−2.00	0.65
		SR-DE-SVM	−0.78	−5.10	−4.30	3.22	−1.79	0.51
$\sigma_{412-215}$	187.4	Monitored	−1.62	−4.37	−5.40	2.36	−2.93	2.57
		SR-DE-SVM	−1.67	−4.46	−5.17	2.09	−2.13	2.34
$\sigma_{412-380}$	192.4	Monitored	−0.52	−2.59	−6.89	0.84	−0.94	1.70
		SR-DE-SVM	−0.49	−2.72	−7.01	0.86	−0.90	1.76
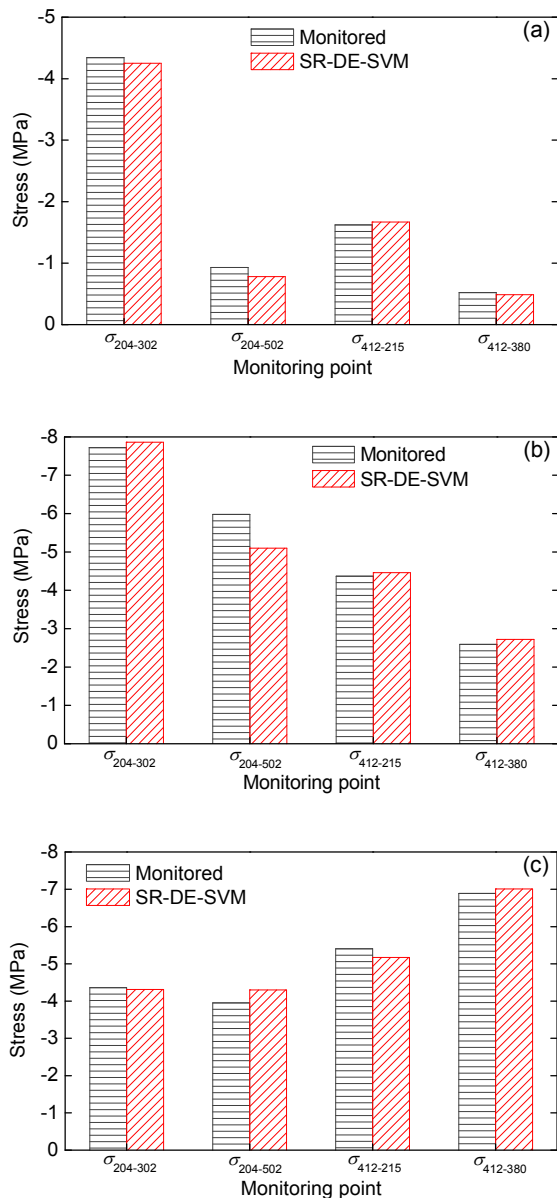
Fig. 16 Comparison of each normal stress at each of the four monitoring points in the Nuozhadu underground cavern group: (a) σ_x; (b) σ_y; (c) σ_z

approach was shown to maintain a consistently high solution accuracy for *in situ* stress estimation, particularly compared with two contemporary approaches, namely, the MLR method and the ANN surrogate direct inversion approach.

With increasing excavation depth, the subsidence trough maintains a single subsiding center throughout excavation in the gravity stress field. However, in the high-level tectonic stress field, the

maximum subsiding center migrates gradually from the primary longitudinal axis to the upstream side of the power house with excavation depth, and the horizontal displacement and its distribution range expand markedly because of the occurrence of the practical tectonic stress field.

In the Huangdeng underground cavern group, the *in situ* stress is moderate and originates mainly from gravity and the geological tectonic stress field. According to the finite element analysis, the category of the surrounding rocks does not have a serious effect on the *in situ* stress field at the engineering site. With increasing rock-mass depth, the normal stresses increase linearly in the area of the underground rock-mass without geological faults and tuff interlayers crossed over in areas.

Validation tests were conducted by comparing the results produced by the SR-DE-SVM algorithm with the measured *in situ* stresses in the Nuozhadu underground cavern groups. The tests showed that the methodology described provides attractive tools to represent the nonlinear relations between boundary conditions and *in situ* stresses in the rock-mass and may be applied to other rock-masses to model the *in situ* stress field. This method can clarify the dominant cause of the formation of *in situ* stress specific to various practical projects to obtain an approximate solution that can provide *in situ* stress information for the design of dams and tunnels.

References

Brown, E.T., Hoek, E., 1978. Trends in relationships between measured *in-situ* stresses and depth. *International Journal of Rock Mechanics and Mining Sciences & Geomechanics Abstracts*, **15**(4):211-215.
http://dx.doi.org/10.1016/0148-9062(78)91227-5

Cheng, M.Y., Hoang, N.D., Wu, Y.W., 2013. Hybrid intelligence approach based on LS-SVM and differential evolution for construction cost index estimation: a Taiwan case study. *Automation in Construction*, **35**:306-313.
http://dx.doi.org/10.1016/j.autcon.2013.05.018

Feng, X.T., Zhang, Z., Sheng, Q., 2000. Estimating mechanical rock mass parameters relating to the three gorges project permanent shiplock using an intelligent displacement back analysis method. *International Journal of Rock Mechanics and Mining Sciences*, **37**(7): 1039-1054.

http://dx.doi.org/10.1016/S1365-1609(00)00035-6

Gong, M., Qi, S., Liu, J., 2010. Engineering geological problems related to high geo-stresses at the Jinping I Hydropower Station, Southwest China. *Bulletin of Engineering Geology and the Environment*, **69**(3):373-380.
http://dx.doi.org/10.1007/s10064-010-0267-1

González de Vallejo, L.I., Hijazo, T., 2008. A new method of estimating the ratio between *in situ* rock stresses and tectonics based on empirical and probabilistic analyses. *Engineering Geology*, **101**(3-4):185-194.
http://dx.doi.org/10.1016/j.enggeo.2008.05.003

Grossberg, S., 1988. Nonlinear neural networks: principles, mechanisms, and architectures. *Neural Networks*, **1**(1): 17-61.
http://dx.doi.org/10.1016/0893-6080(88)90021-4

Guo, H.Z., Ma, Q.C., Xue, X.C., *et al.*, 1983. The analytical method of the initial stress field for rock masses. *Chinese Journal of Geotechnical Engineering*, **5**(3):64-75 (in Chinese).

Guo, M.W., Li, C.G., Wang, S.L., *et al.*, 2008. Study on inverse analysis of 3-D initial geostress field with optimized displacement boundaries. *Rock and Soil Mechanics*, **29**(5):1269-1274 (in Chinese).

Hijazo, T., González de Vallejo, L.I., 2012. *In-situ* stress amplification due to geological factors in tunnels: the case of Pajares tunnels, Spain. *Engineering Geology*, **137-138**:13-20.
http://dx.doi.org/10.1016/j.enggeo.2012.03.007

Jiang, A., Zhao, H., Jiang, S., 2013. Study on 3D intelligent back analysis of tunnel based on DE-SVM. *Chinese Journal of Underground Space and Engineering*, **9**(4): 765-770 (in Chinese).

Jiang, Q., Feng, X.T., Chen, J.L., *et al.*, 2008. Nonlinear inversion of 3D initial geostress field in Jinping II Hydropower Station region. *Rock and Soil Mechanics*, **29**(11):3003-3010 (in Chinese).

Kartam, N., Flood, I., Garrett, J.H., 1997. Artificial Neural Networks for Civil Engineers: Fundamentals and Applications. American Society of Civil Engineers, New York, USA.

Li, Y.S., Yin, J.M., Chen, J.P., *et al.*, 2012. Analysis of 3D *in-situ* stress field and query system's development based on visual BP neural network. *Procedia Earth and Planetary Science*, **5**:64-69.
http://dx.doi.org/10.1016/j.proeps.2012.01.011

Liu, Y., Li, H., Luo, C., *et al.*, 2014. *In situ* stress measurements by hydraulic fracturing in the western route of south to north water transfer project in China. *Engineering Geology*, **168**:114-119.
http://dx.doi.org/10.1016/j.enggeo.2013.11.008

Mckinnon, S., 2001. Analysis of stress measurements using a numerical model methodology. *International Journal of*

Rock Mechanics and Mining Sciences, **38**(5):699-709.
http://dx.doi.org/10.1016/S1365-1609(01)00037-5

Qin, Z., Liu, C., Zhao, Z., *et al.*, 2008. Back analysis of inintial ground stress by 3D-FSM considering influence of terrain and tectonic stress. *Rock and Soil Mechanics*, **7**:027 (in Chinese).

Saati, V., Mortazavi, A., 2011. Numerical modelling of *in situ* stress calculation using borehole slotter test. *Tunnelling and Underground Space Technology*, **26**(1):172-178.
http://dx.doi.org/10.1016/j.tust.2010.07.002

Samui, P., Kim, D., Aiyer, B.G., 2015. Pullout capacity of small ground anchor: a least square support vector machine approach. *Journal of Zhejiang University-SCIENCE A (Applied Physics & Engineering)*, **16**(4): 295-301.
http://dx.doi.org/10.1631/jzus.A1200260

Xing, B., Zhang, K., Sun, S., *et al.*, 2015. Emotion-driven Chinese folk music-image retrieval based on DE-SVM. *Neurocomputing*, **148**:619-627.
http://dx.doi.org/10.1016/j.neucom.2014.08.007

Xu, R.Q., 2000. The GA-ANN method for determining calculation parameters for deep excavation. *Journal of Zhejiang University-SCIENCE*, **1**(4):408-413.
http://dx.doi.org/10.1631/jzus.2000.0408

Xue, L., Chen, S., 2006. Two-stage analysis of geostress field for underground chamber area of Pubugou project. *Chinese Journal of Rock Mechanics and Engineering*, **25**(9):1881-1886 (in Chinese).

Zhang, L., Yue, Z., Yang, Z., *et al.*, 2006. A displacement-based back-analysis method for rock mass modulus and horizontal *in situ* stress in tunneling–illustrated with a case study. *Tunnelling and Underground Space Technology*, **21**(6):636-649.
http://dx.doi.org/10.1016/j.tust.2005.12.001

Zhang, S., Yin, S., 2014. Determination of *in situ* stresses and elastic parameters from hydraulic fracturing tests by geomechanics modeling and soft computing. *Journal of Petroleum Science and Engineering*, **124**:484-492.
http://dx.doi.org/10.1016/j.petrol.2014.09.002

Zhang, Z.M., 2011. Achievements and problems of geotechnical engineering investigation in China. *Journal of Zhejiang University-SCIENCE A (Applied Physics & Engineering)*, **12**(2):87-102.
http://dx.doi.org/10.1631/jzus.A1000433

Zhao, D., Chen, Z., Cai, X., *et al.*, 2007. Analysis of distribution rule of geostress in China. *Chinese Journal of Rock Mechanics and Engineering*, **26**(6):1265-1271 (in Chinese).

Zhao, H., Ma, F., Xu, J., *et al.*, 2012. *In situ* stress field inversion and its application in mining-induced rock mass movement. *International Journal of Rock Mechanics and Mining Sciences*, **53**:120-128.
http://dx.doi.org/10.1016/j.ijrmms.2012.05.005

中文概要

题　目： 大型地下洞室群区域三维地应力场二次反演分析

目　的： 地下洞室群区域地应力分布繁杂多变，勘测点因数量有限难以反映初始地应力场空间分布特征。考虑工程区域内的地质构造、地形地貌及河谷的发育演化史等因素，提出综合反映工程区复杂地质条件及地层剥蚀过程的地应力场二次反演方法，揭示工程所在区域的三维地应力场分布特征，为地下工程的开挖加固设计提供更加准确的基础资料。

创新点： 1. 基于地应力场反演基本理论，建立逐步回归-差异进化-支持向量机模型（SR-DE-SVM）的二次反演非线性模型；2. 通过 SR-DE-SVM 算法计算流程，成功模拟工程区域地应力场分布。

方　法： 1. 通过工程勘测分析，推导出构造运动对工程区域地应力场分布产生的影响（表 5 和图 13）；2. 基于智能反演方法，构建 SR-DE-SVM 的二次反演非线性模型（公式（10）），得到 SR-DE-SVM 算法的计算流程（图 2）；3. 通过数值仿真模拟，结合地质历史的发展过程，验证所提出的二次反演方法的可行性和有效性（图 10 和 11）。

结　论： 1. 工程区域内初始地应力水平属中等，主要受到岩体自重与构造运动的双重影响。2. SR-DE-SVM 二次反演方法可更加清楚地明确初始地应力形成的主导成因，且更加准确、高效和真实地模拟工程区域三维地应力场的分布规律；3. 围岩类别对黄登地下洞室群区域内的初始地应力场影响不大，仅在断层带及 III、IV 类凝灰岩夹层带切割部位有显著的应力释放效应。

关键词： 初始地应力；逐步回归；支持向量机；差异进化；有限元；黄登地下洞室